COMMUNICATION

Check for updates

Porous silicon biosensors meet zwitterionic peptides: tackling biofouling from proteins to cells

Kayan Awawdeh,[a] Xin Jiang,[a] Lisa Dahan,[a] Matan Atias,[a] Janina Bahnemann [iD][bc] and Ester Segal [iD] *[a]

Porous silicon (PSi)-based biosensors are promising platforms for label-free biomarker detection in complex environments, including potential *in vivo* applications, but their use remains limited due to their susceptibility to biofouling caused by their high surface area. Here, we address this challenge by covalently immobilizing zwitterionic peptides with glutamic acid (E) and lysine (K) repeating motifs onto PSi thin films. Systematic screening identified a specific sequence, EKEKEKEKEKGGC, which exhibited superior antibiofouling properties compared to conventional polyethylene glycol (PEG) coatings. This peptide effectively prevented nonspecific adsorption of biomolecules from complex biofluids, including gastrointestinal (GI) fluid and bacterial lysate. Applying this strategy to a PSi-based aptasensor for lactoferrin detection, we achieved more than one

New concepts

This work presents the first application of zwitterionic peptides specifically tailored for porous silicon (PSi), enabling the development of a high-performance aptasensor capable of operating in complex biological fluids. Unlike conventional antibiofouling strategies, the short zwitterionic peptide forms a stable, charge-neutral hydration layer that effectively resists non-specific adsorption while preserving the surface functionality required for selective aptamer coupling. Beyond protein fouling, the peptide provides broad-spectrum resistance to cellular adhesion, including biofilm-forming bacteria and mammalian cells. By demonstrating reliable, label-free sensing performance in highly challenging media, this platform introduces a new strategy for surface engineering of PSi biosensors and expands their applicability to clinically relevant environments and implantable devices.

[a] Department of Biotechnology and Food Engineering, Technion – Israel Institute of Technology, 3200003 Haifa, Israel. E-mail: esegal@technion.ac.il

[b] Institute of Physics, University of Augsburg, 86159 Augsburg, Germany

[c] Centre for Advanced Analytics and Predictive Sciences (CAAPS), University of Augsburg, 86159 Augsburg, Germany

order of magnitude improvement in both the limit of detection and (LOD) and signal to noise ratio over PEG-passivated sensors, enabling sensitive detection in clinically relevant concentration ranges. The peptide's antibiofouling performance was also extended to biofilm-forming bacteria and adherent mammalian cells, underscoring its broad-spectrum protection against both molecular and cellular contamination. This universal strategy enhances the reliability of PSi biosensors by addressing a key cause of sensor failure in real-world applications.

I have served on the Nanoscale Horizons Advisory Board since 2020 and published my first paper in the journal in 2022. This work focuses on nanostructured materials for biosensors, while my group also develops responsive delivery systems and hybrid materials to address global challenges. What I particularly value about Nanoscale Horizons is its emphasis on new concepts, making it a unique platform for advancing the field. My warmest congratulations on the journal's 10th anniversary, and to many more exciting studies ahead.

Ester Segal

Introduction

The phenomenon of biofouling poses a significant challenge within biosensors, since it generates elevated background signals that are difficult to distinguish from specific binding signals.[1,2] Accordingly, when developing a biosensor, it is essential to ensure that it can effectively concentrate the target analyte from the solution onto its surface without evoking non-specific interactions with interfering biomolecules present in the biological fluid, as these background signals compromise the biosensor's dynamic detection range, limit of detection (LOD), and reproducibility.[3]

Porous silicon (PSi)-based biosensors have gained significant attention in recent years due to their high surface area, tunable pore size, and ability to facilitate label-free optical and electrochemical sensing;[4] however, the porous nature of these structures also increases their susceptibility to biofouling, particularly with respect to complex biological media, such as body fluids and cell lysates.[5–8] The extent of this phenomenon in PSi biosensors is governed by the interplay between the transducer's pore size and surface chemistry, and the physicochemical properties of both the target and interfering molecules.[9,10] While small pores increase the surface area, they can serve as effective molecular filters, preventing the infiltration of large biomolecules and as such reduce non-specific binding. Large pores despite offering a reduced surface area are comparatively more prone to fouling.[11–16]

Since protein biomarkers are the most common clinically relevant targets,[17,18] understanding their adsorption on biosensor surfaces is crucial for minimizing non-specific binding and improving sensor performance. Protein adsorption at interfaces involves complex and dynamic interactions that are influenced by environmental conditions such as pH, ionic strength, and temperature.[1,2,19,20] In solution, proteins rotate freely and can adapt their orientation based on surface properties,[1,2,19,20] and they tend to expose hydrophilic regions to hydrophilic surfaces and hydrophobic regions to hydrophobic surfaces.[3,20] Similarly, proteins can also orient their charged regions to interact with oppositely charged surfaces, allowing net positively or negatively charged proteins to adsorb to surfaces with similar overall charges.[1,2,19,20]

In order to overcome non-specific adsorption and minimize biofouling in PSi biosensors, several strategies have been employed.[7,21,22] These strategies primarily involve the use of inert blocking agents, which operate through either physical adsorption or covalent binding. After the immobilization of the capture probe, a blocking step is typically carried out to prevent the non-specific binding of undesired non-target biomolecules. The most common blocking strategies deployed with respect to PSi surfaces rely on the conjugation of small hydrophilic passivation molecules, like ethanolamine[23] and Tris,[6,24] in addition to the use of polyethylene glycol (PEG) of varying molecular weights,[6,25] gelatin,[26] or bovine serum albumin (BSA).[6] These molecules can tightly bind water via hydrogen and/or electrostatic interactions forming a strong hydration layer that acts as a physical and energetic barrier to adsorption.[27] PEG has long served as the "gold-standard" and been extensively studied – yet PEG molecules are prone to oxidative degradation in biological media. Hyperbranched polyglycerol (HPG), an analog to PEG with a hyperbranched architecture, has also been studied on PSi surfaces[28] as a promising alternative. It offers superior thermal and oxidative stability compared to PEG, along with enhanced hydrophilicity and surface coverage due to its three-dimensional, multi-terminal hydroxyl group structure.[3,27] Yet, despite these advantages, the polymerization process of HPGs is difficult to control, due to increased viscosity during polymerization.[29] Another promising strategy relies on thermal carbonization of porous silicon (TCPSi), resulting in the

formation of a Si–C layer.[30–33] The latter improves the stability and functionality of the biosensor in biological environments.[30–33] TCPSi surfaces can also be functionalized with standard coatings, such as PEG derivatives, to further enhance antifouling properties.[34] Yet, excessive carbonization can lead to black carbonaceous deposits that diminish optical interference fringes, cause pore blockages and reduce porosity, impairing biosensing performance.[35]

Zwitterionic materials, possessing both positive and negative residues, are net-neutral and highly effective for surface passivation of biosensors.[36,37] Their antibiofouling properties arise from two key features: the net-neutral surface minimizes electrostatic interactions with biomolecules, while the opposing charges tightly bind water molecules to form a strong hydration layer.[36,37] This layer, stabilized by both hydrogen and electrostatic bonding, serves an effective barrier against non-specific adsorption, offering superior antifouling performance over PEG.[27,38] Zwitterionic materials have been widely studied in the context of porous scaffolds.[39] For example, zwitterionic phospholipids have been incorporated into nanoporous gold substrates,[40] and zwitterionic polymers have been grafted onto thermally hydrosilylated PSi for the first time to address hydrolysis and fouling issues.[41]

Among zwitterionic materials, zwitterionic peptides have emerged as particularly promising candidates for preventing biofouling and enabling reliable detection of biomarkers.[42–45] Beside their biocompatibility and bioinert nature, they offer several advantages: they can be commercially synthesized, and their sequence and length can be easily controlled and tuned to optimize surface passivation and enhance biosensor performance.[46–48]

The most studied zwitterionic peptides consist of lysine and glutamic acid (EK) amino acid repetitions with a cysteine end allowing for their facile conjugation onto different surfaces, with the zwitterionic structure facing toward the bulk solution.[47,48] Moreover, zwitterionic peptides have demonstrated significant potential not only in preventing protein adsorption, but also with respect to both bacterial and mammalian cell adhesion.[37,45,49–51]

Here, we investigate the use of surface-tethered zwitterionic peptides containing EK motifs for minimizing non-specific binding in PSi-based aptasensors. We systematically evaluate the efficacy of different zwitterionic peptide sequences in preventing protein and biofluid adsorption. The most effective sequence is employed in an aptasensor for the detection of lactoferrin (LF), a protein biomarker for gastrointestinal (GI) inflammatory disorders, in GI fluids. This allows us to investigate how peptide influences both antifouling performance and biosensing functionality. We further explore the broader potential of this zwitterionic peptide in preventing biofouling with model microorganisms and mammalian cells onto PSi. This work bridges surface chemistry optimization and biosensor design, addressing critical challenges in real-world applications, such as biomarker detection in complex physiological fluids.

Results and discussion

The antibiofouling properties of five different amino acid sequences, as summarized in Table 1, were characterized. Each

Table 1 Characteristics of the studied peptides in terms of sequence, molecular weight, and isoelectric point

Number	Sequence	Molecular weight (Da)	Isoelectric point
1	EKEKEKEKEKGGC	1563	6.7
2	EEKKEEKKEKGGC	1563	6.7
3	ERERERERERGGC	1589	6.7
4	KSESKSESKEGGC	1396	6.54
5	TSTSTSTSTSGGC	1217	n/a

peptide consists of three elements: (i) an antifouling segment, (ii) a spacer composed of two glycine (G) residues, and (iii) a terminal cysteine (C), that serves as an anchoring group, enabling facile conjugation onto the PSi surface in an appropriate orientation with the antifouling segment facing outward. Among these, three peptides (1, 2, and 4) were designed with repeating motifs of glutamic acid (E) and lysine (K), which carry negative and positive charges, respectively, at physiological pH, arranged in different sequence patterns. Specifically, peptide 1 consists of alternating EK repeats; peptide 2 consists of block-charged E_2K_2 repeats; and peptide 4 incorporates hydrophilic serine (S) residues as spacers between each E and K, forming ESKS repeats. The design of these sequences was based on previous studies showing that peptides composed of repeating E and K amino acids exhibit enhanced resistance to non-specific adsorption, owing to their strong interaction with water molecules, as well as their neutrality, which minimizes electrostatic interactions with the surface.[50–54] In addition, we evaluated peptide 3, which features alternating E and arginine (R), a positively charged amino acid at physiological pH, as an alternative to lysine. For comparison, an uncharged, hydrophilic peptide (peptide 5) composed of threonine (T) and serine (S) residues, as well as the "gold standard" PEG molecules (750 Da, comparable in length to the peptides), were included.

Characterization of peptide conjugation onto the PSi surface

The peptides were conjugated to the nanostructured PSi scaffolds (see Fig. S1 for the corresponding SEM images, SI) *via* a maleimide-NHS crosslinking reaction as illustrated in Fig. 1A. The cysteine thiol group of the peptide covalently binds to the amino-silanized PSi surface. This process was characterized using Fourier transform infrared (FTIR) spectroscopy, with spectra recorded after each step (Fig. 1B). Following amino-silanization of the oxidized PSi, a peak at 1634 cm^{-1}, attributed to primary amines, was observed.[24] Subsequent activation of the surface with the EMCS crosslinker introduced two new peaks at 1552 and 1654 cm^{-1}, corresponding to amide II and amide I bonds, respectively, along with a new peak at 1706 cm^{-1}, assigned to the C=O stretching vibrations of maleimide groups.[24] After peptide conjugation, the intensity of the peaks of both amide I and II bonds was observed to increase due to the amide bonds in the backbone of the immobilized peptides. In addition, to further characterize the peptide conjugation process, FAM6-labeled peptide 1 was robotically microspotted onto three different substrates: (i) EMCS-activated surface, (ii) amino-silanized PSi omitting EMCS activation, and (iii) bare
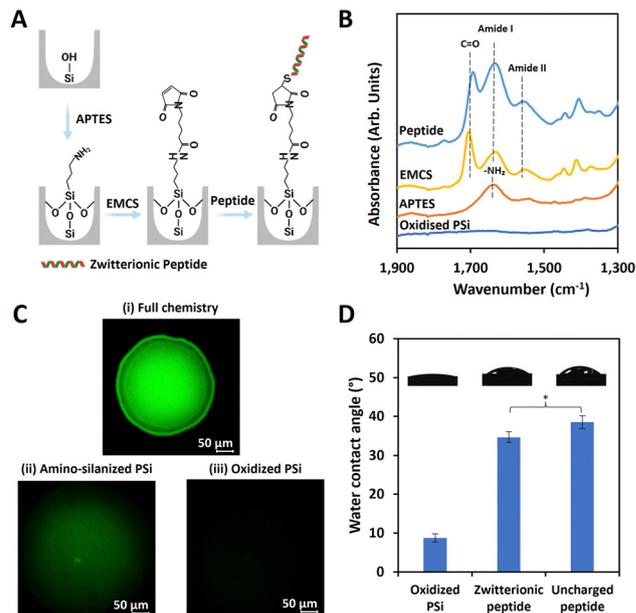

Fig. 1 Characterization of peptide conjugation on the PSi surface. (A) Schematic illustration of zwitterionic peptide immobilization onto the PSi surface. Created with https://BioRender.com. (B) ATR-FTIR spectra. (C) CLSM projection images of the PSi film conjugated with a FAM6-labeled peptide in the following cases: (i) full conjugation chemistry, (ii) control experiment with no activation of the silanized surface with the coupling agent EMCS and (iii) bare oxidized PSi. Data represented as means ± SD, n = 3. (D) The static water contact angle measurement on the different modified surfaces; oxidized PSi, zwitterionic peptides and uncharged peptides modified surfaces.

oxidized PSi. The peptide was incubated for 1 h and thoroughly washed with PBS to remove unbound peptides. Fluorescence micrographs of the resulting surfaces are shown in Fig. 1C. When the full peptide conjugation process was employed (as depicted in Fig. 1A), a strong fluorescence signal was observed within the spotted area (∼300 μm in diameter; Fig. 1C-i), indicating covalent immobilization of the peptide *via* an EMCS crosslinker.[55–57] In contrast, the control lacking EMCS activation exhibited only weak fluorescence (Fig. 1C-ii), which we attribute to non-specific adsorption of the FAM6 labeling dye onto the silanized PSi surface, possibly due to electrostatic interactions between the negatively charged FAM label and the protonated amines on the APTES-modified PSi surface (at neutral pH). No detectable fluorescence was observed on bare oxidized PSi (Fig. 1C-iii), thereby confirming that surface functionalization is required for covalent and effective peptide immobilization onto the PSi nanostructure.

We also measured the water contact angle of the peptide-immobilized PSi, and the results are depicted in Fig. 1D. Conjugation of the zwitterionic peptide (peptide 1) significantly increased (by ∼4-fold) the contact angle compared to the neat PSi, confirming successful peptide immobilization. The measured contact angle of 35° indicates that the surface remained highly hydrophilic, consistent with previously reported values for zwitterionic peptide-modified surfaces.[42,58] For comparison, PSi conjugated with an uncharged hydrophilic peptide (peptide

5) exhibited a statistically higher contact angle of 38°, attributed to the absence of charged amino acid residues. Successful conjugation was further confirmed by monitoring changes in the reflectivity spectra of PSi during peptide immobilization (see Fig. S2, SI). Additionally, peptide surface density within the PSi nanostructure was determined *via* fluorescence-based cleavage assay using FAM-labeled peptides, yielding a calculated surface density of 3.16×10^{13} molecules cm^{-2}, indicative of efficient immobilization within the porous nanostructures (Table S1, SI).

Protein adsorption

Protein adsorption on the modified PSi was evaluated using reflective interferometric Fourier transform spectroscopy (RIFTS), which enables real-time monitoring of surface interactions. In this method, the reflectivity spectra of PSi were recorded, and the corresponding effective optical signal (EOT) values were calculated. The latter correlates with changes in the refractive index of the porous structure, where increases in EOT indicate an increase in the refractive index, which is proportional to the amount of accumulated biomolecules within the porous structure. To assess the antibiofouling performance of the different peptide sequences, the modified surfaces were exposed to 1 mg mL^{-1} solutions of three different proteins: LF, anterior gradient homolog-2 (AGR2), and BSA. These proteins were selected for their diverse structural properties, varying molecular sizes (ranging from 22 to 87 kDa), and charges at neutral pH. An initial baseline was established in PBS, followed by 1-hour incubation with protein solutions and a PBS wash to remove loosely bound proteins. The results are presented as the net relative EOT changes ($\Delta EOT/EOT_0$) and are summarized in Fig. 2A.

The oxidized PSi exhibited high levels of protein adsorption, with $\Delta EOT/EOT_0$ values reaching $\sim 30 \times 10^{-3}$ for both LF and AGR2, attributed to electrostatic interactions between the positively charged proteins and the negatively charged oxidized PSi surface.[59] The adsorption of BSA, which carries a net negative charge at neutral pH, was significantly lower ($\sim 5 \times 10^{-3}$), likely due to localized positively charged regions of the protein that can interact with the surface.[20] All peptide-immobilized surfaces showed significant reduction in protein adsorption compared to the bare oxidized PSi. Among the studied peptides, peptide 1-immoblized PSi was resistant to protein adsorption, as shown in Fig. 2A, attributed to the formation of a strong hydration layer and an overall net-neutral surface charge.[50–53] Notably, peptide 1 outperformed the "gold standard" PEG-modified surface, underscoring the importance of both surface charge neutrality and hydration layer formation in achieving superior antifouling performance. Peptide 2, containing block-charged E_2K_2 repeats, exhibited negligible LF and BSA (positively and negatively charged proteins, respectively) adsorption, ascribed to reduced electrostatic interactions and overall surface neutrality. In the case of AGR2 (22 kDa, positively charged), adsorption was observed, although profoundly lower compared to oxidized PSi, indicating poor resistance to this protein. This may be attributed to the charge distribution of peptide 2, which likely promotes looped rather than linear conformations (as
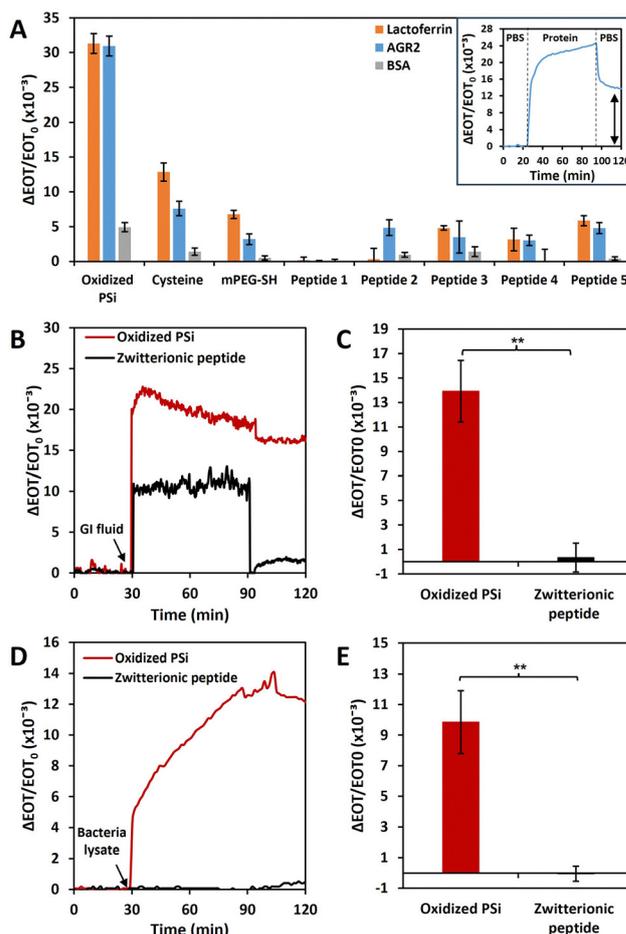

Fig. 2 Protein and bio-fluid adsorption: (A) net relative EOT changes of the modified PSi films after incubation with the different proteins (lactoferrin, AGR2, and BSA, each at a concentration of 1 mg mL^{-1}). The inset shows a representative real-time EOT curve and the corresponding net EOT changes. (B) Real-time EOT changes and (C) average net relative EOT changes upon exposure of the modified surface to the GI fluid (a total protein concentration of 10 mg mL^{-1}). (D) Real-time EOT changes and (E) average net relative EOT changes upon exposure of the modified surface to the bacterial lysate (a total protein concentration of 2.5 mg mL^{-1}). (** indicates statistical significance; *t*-test, $n \geq 3$, $p < 0.05$).

peptide 1), thereby reducing the density of the hydration layer and rendering the surface more susceptible to adsorption of small proteins like AGR2.[20,48,54,60] Peptide 3-immobilized PSi remained prone to adsorption of all three proteins, despite reducing overall adsorption compared to oxidized PSi. This is likely due to arginine's guanidinium group, which forms a weaker hydration layer and promotes interactions with other amino acids, particularly hydrophobic residues.[48,53] Peptide 4 exhibited similar performance to peptide 3, with no statistical significance, which may arise from disrupted charge uniformity and a weaker hydration/electrostatic barrier.[61] Peptide 5, an uncharged hydrophilic peptide, exhibited antibiofouling performance comparable to PEG-modified PSi, attributed to its ability to form a hydration layer. However, similar to PEG, the absence of charged residues limits electrostatic repulsion, leaving it susceptible to non-specific interactions.[62] The

immobilized zwitterionic peptides exhibited superior antibiofouling performance compared to PEG-amine and Tris, both of which were similarly grafted onto the PSi surface *via* conventional carbodiimide coupling (NHS/EDC), widely used in PSi-based biosensors[6,24,25,63] (Fig. S3, SI).

The superior antibiofouling behaviour of peptide 1 was also demonstrated on planar silicon oxide surfaces by quartz crystal microbalance (QCM) measurements. The peptide was immobilized onto the silicon oxide sensors and exposed to 1 mg mL^{-1} LF in PBS (Fig. S4, SI). No LF adsorption was detected on the peptide 1-immoblized sensor; whereas for peptide 5- and PEG-immobilized sensors comparable LF adsorption levels were attained. In contrast, the bare oxidized silicon displayed significantly higher adsorption. These results are consistent with those observed for the porous surfaces.

To provide a molecular-level insight, we predicted the secondary structures of the studied peptides using AlphaFold 3[64] software (Fig. S5, SI). Peptides 1–3 adopted α-helical conformations, whereas peptides 4 and 5 are more disordered. The α-helical arrangement allows for tighter molecular packing, resulting in enhanced steric repulsion to prevent biofouling.[50,52,65,66] To further examine the peptide–water interactions, we calculated the solvent-accessible surface area (SASA) values, using ChimeraX software,[67] representing the surface available for solvent contact.[68,69] Peptide 1 is found to exhibit the largest solvent-exposed area (1766.5 Å^2), compared to ~1610–1726 Å^2 for the other peptides (results presented in Table S2, SI). Although the SASA value does not directly quantify hydration strength, the greater solvent exposure of the helical zwitterionic peptides supports their ability to form dense hydration shells, thereby suppressing biofouling. These observations align with our experimental results, which show that peptide 1 exhibits the strongest antibiofouling activity.

Next, the antibiofouling behavior of peptide 1-immobilized PSi was characterized upon exposure to complex biological media. We used real GI fluids and bacterial lysates, having protein contents of 10 mg mL^{-1} and 2.5 mg mL^{-1}, respectively. Unlike buffer-based assays, these tests reflect biologically relevant conditions that better mimic real-world biosensing environments. Fig. 2B shows a representative real-time EOT response for peptide-immobilized and bare oxidized PSi surfaces upon exposure to the GI fluid with the corresponding net EOT changes summarized in Fig. 2C. Upon the introduction of the GI fluid, an increase in the EOT signal was observed in both cases. However, after PBS washing, the EOT signal for the peptide-modified surface decreased significantly, inducing only a negligible signal. Similarly, Fig. 2D and E present the real-time and net EOT changes, respectively, upon exposure to bacterial lysate. In this case, no increase in the EOT signal was observed for the peptide-modified surface throughout the measurement. These results demonstrate the effectiveness of peptide 1 in resisting non-specific adsorption in complex biological media. Hence, it was employed as the antifouling agent in the biosensor construction and all subsequent experiments.

Aptasensor construction and biosensing performance

For biosensor construction, the PSi surface was first amino-silanized and subsequently activated with EMCS, as we

previously described. Thiol-terminated Lac 9-2[70] aptamers (specific for LF detection) were conjugated onto the modified PSi, followed by peptide 1 immobilization as illustrated in Fig. 3A. This process was monitored in real time using RIFTS and the results are depicted in Fig. 3B. After establishing a baseline with PBS on the aminated PSi, the introduction of EMCS induced a rapid increase in EOT, corresponding to the covalent attachment of the crosslinker within the porous layer. Subsequent addition of the aptamer and peptide 1 each led to a further increase in EOT. After each step, the modified surface was thoroughly washed with PBS to remove unbound molecules; notably, no decrease in the EOT signal was observed, confirming the successful covalent attachment to PSi. Moreover, aptamer conjugation was characterized by confocal laser scanning microscopy (CLSM), where z-stack images were acquired over a depth of ~3 μm (corresponding to the PSi thickness according to SEM measurements, see Fig. S1, SI). Cy5-labeled aptamers were conjugated to the PSi surface, and the resulting 3D projection of the PSi films are shown in Fig. 3C. A uniform fluorescence signal is observed throughout the porous layer (Fig. 3C-ii), when the full chemistry of the labeled aptamer was utilized. In contrast, no fluorescence signal is detected on the control surface, where the APTES-modified PSi was incubated with the labeled aptamer without prior EMCS activation (Fig. 3C-i).

The selectivity of the resulting aptasensor was studied upon exposure to various protein solutions (90 μg mL^{-1} in selection buffer, SB), as shown in Fig. 4A. The aptasensor exhibited no measurable response to clinically relevant non-target proteins, including AGR2, BSA, and trypsin, confirming negligible non-specific adsorption. In contrast, exposure to the target protein, LF, resulted in a distinct and significant increase in EOT, indicating a strong and specific interaction with the immobilized aptamers. Compared to our previously reported aptasensor in which carbodiimide chemistry was employed for the immobilization of the Lac 9-2 aptamer with PEG passivation,[15] the current biosensor design demonstrated a substantially improved signal-to-noise ratio (SNR). While maintaining comparable EOT signal levels, the new aptasensor achieved an SNR of 40 for LF, *versus* 0.4–1.7 for non-target proteins. This improvement underscores the zwitterionic layer's function in reducing non-specific adsorption, resulting in improved selectivity.

To evaluate the biosensing performance in physiologically relevant complex media, experiments were conducted in the GI fluid, a heterogeneous mixture containing high concentrations of non-target biomolecules (Fig. 4B). Initially, the aptasensor was first incubated in the neat GI fluid to establish a stable baseline, followed by exposure to the GI fluid spiked with the target molecule (LF, 1 μM) for 1 h. Subsequently, the sensor was washed with fresh GI fluid to remove unbound LF. Fig. 4B shows that the net relative EOT change achieved with the aptasensor exceeds that of the previously reported PEG-passivated counterpart.[15] Importantly, exposure to the neat GI fluid induced only negligible EOT changes, demonstrating the biosensor's superior resistance to biofouling compared to the PEG-passivated sensor (Fig. 4B).
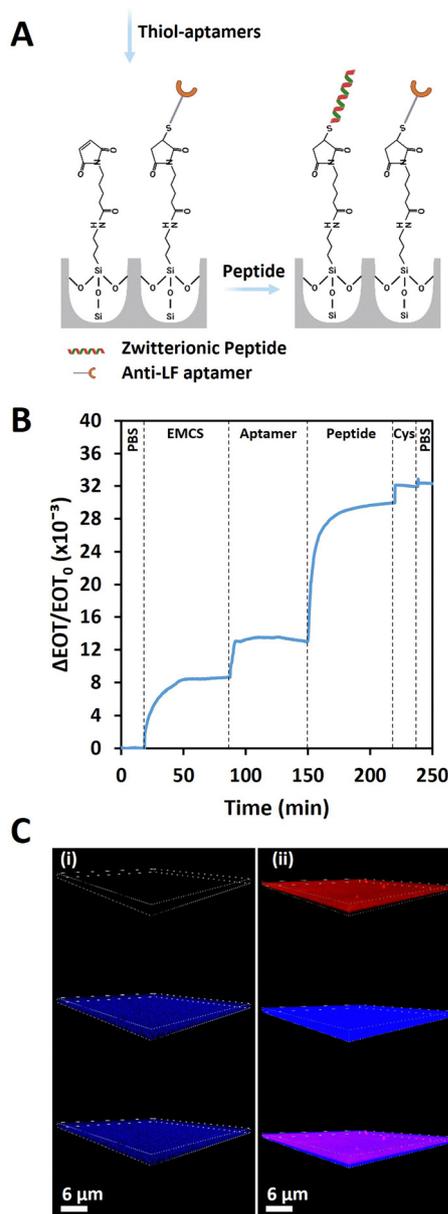
Fig. 3 Biosensor construction: (A) schematic illustration of thiol-terminated aptamer and zwitterionic peptide immobilization onto the PSi surface. Created with **https://BioRender.com**. (B) Relative EOT changes of the PSi film following the immobilization of peptides: amino-silanization with APTES, activation with EMCS, immobilization of thiol-terminated aptamers and passivation with the peptides. (C) CLSM projection images of the PSi film conjugated with a Cy5-labeled aptamer in the following cases: (i) control experiment with no activation of the silanized surface with the coupling agent EMCS and (ii) full conjugation chemistry. The top row represents the fluorescence signal of the Cy5-labeled aptamer, the middle row represents the PL of the PSi nanostructure, and the bottom row is the merged view of the top and middle rows.

Fig. 4 Biosensor performance: (A) real-time relative EOT changes upon introduction of the target protein LF (90 μg mL^{-1}, equivalent to 1 μM) and other non-target proteins (AGR2, BSA and trypsin) at a similar concentration in buffer. (B) Net relative EOT changes in response to the LF-spiked GI fluid (1 μM) comparing the zwitterionic peptide-modified aptasensor with the PEG-passivated biosensor. (C) Baseline comparison in the neat GI fluid. (D) LF binding curve in the GI fluid over a concentration range of 0.05 to 1 μM (n = 3). (E) Illustration of the micro-impeller system, consisting of a mixing chamber for the impeller and a measurement zone with a height of 1 mm. (F) Characteristic real-time EOT changes for the micro-impeller system upon introduction of the LF-spiked GI sample at concentrations of 10 and 50 nM LF.

Fig. 4D shows the biosensor binding curve in the GI fluid, revealing a linear correlation between the net EOT change signal and the LF concentration within the range of 0.05 to 1 μM (R^2 = 0.9609). The LOD was calculated to be 49 nM, more than one order of magnitude lower than that of the previously reported PEG-passivated aptasensor.[15] In fact, this LOD is comparable to that of the PEG-passivated sensor in buffer, underscoring the crucial impact of zwitterionic peptide modification in enhancing overall biosensor performance in complex media and enabling reliable detection of target analytes in complex clinical samples.

To further enhance the LF-biosensor sensitivity towards clinically relevant concentrations ($>$10 nM, as reported for patients[71–75]), the biosensor was integrated into a microfluidic device incorporating a micro-impeller (Fig. 4E), previously

The zwitterionic layer also contributed to reducing the background noise in the GI fluid, as evidenced by the baseline relative EOT changes presented in Fig. 4C. As a result, the biosensor's characteristic SNR increased by more than an order of magnitude compared to the PEG-passivated aptasensor.
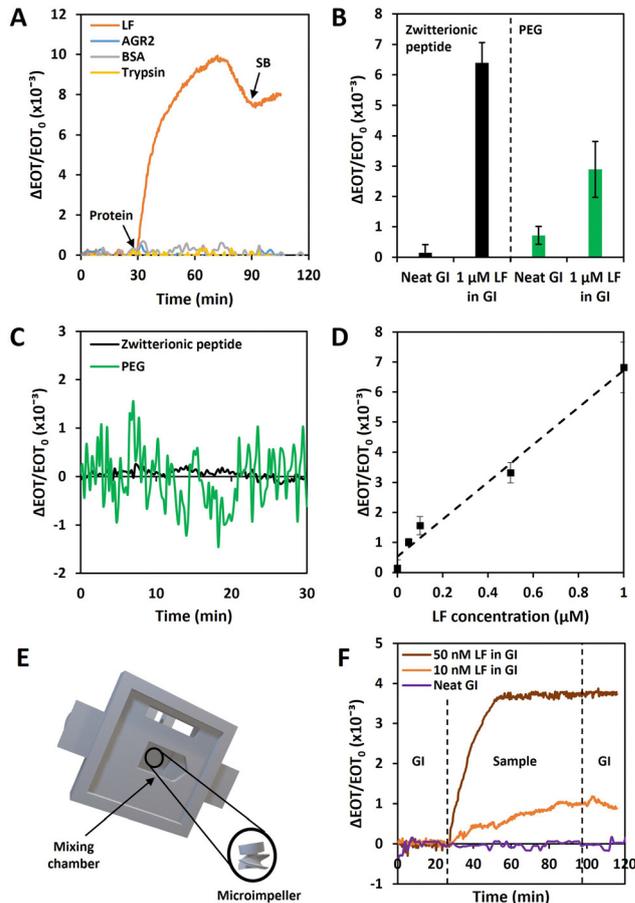
developed in our lab,[15] enabling active mixing, reduced depletion zones, and improved mass transport and detection performance. The integrated biosensor was exposed to low concentrations of LF (10 and 50 nM), with real-time EOT changes presented in Fig. 4F, demonstrating a clear significant signal increase at both levels. This confirms the successful and reliable detection of clinically relevant LF concentrations in complex media. Note that despite the enhanced flux induced by this micro-impeller design, the signal upon exposure to the neat GI fluid (Fig. 4F) remained stable, indicating effective suppression of non-specific adsorption even under active mixing conditions.

Cellular biofouling resistance

Cellular biofouling is a major challenge for PSi biosensors, both for *in vivo* use and when analyzing clinical samples containing non-target cells (bacterial or mammalian), where unintended cell adhesion may impair sensor performance and reliability.[4,76,77] Hence, we studied the antibiofouling performance of zwitterionic peptide-immobilized PSi in rich bacterial suspensions and mammalian cell cultures.

To assess bacterial attachment and colonization, the zwitterionic PSi films were incubated for 24 hours at 37 °C with two model bacteria, *Escherichia coli* (*E. coli*) and *Staphylococcus saprophyticus* (*S. saprophyticus*). These species represent clinically relevant Gram-negative and Gram-positive bacteria commonly associated with biofilm formation on implantable medical devices.[78–81] Following incubation, films were washed to remove loosely bound bacteria, stained with the Syto9 dye and imaged by fluorescence microscopy (Fig. 5). Both strains adhered strongly to bare oxidized PSi, with *E. coli* forming a highly dense bacterial layer (Fig. 5A), likely due to the differences in their membrane composition and structure.[82] Lipopolysaccharides, abundant in the outer membrane of Gram-negative bacteria, were shown to assist in their adhesion to negatively charged surfaces, such as oxidized PSi.[59,83] In contrast, the zwitterionic peptide-modified PSi surfaces displayed remarkable resistance to bacterial attachment, where only few *E. coli* cells were observed and none for *S. saprophyticus* (Fig. 5C and D, respectively).

We next evaluated the ability of the zwitterionic PSi surfaces to resist mammalian cell adhesion. In these experiments, PSi chips with 20 nm pore diameters were selected (see Fig. S1, SI), as their surface roughness is known to promote mammalian cell attachment.[84] Two cell lines, MRC5 (human lung fibroblasts) and BxPC-3 (human pancreatic cancer cells), were selected for their known tendency to adhere strongly to various surfaces, making them suitable models for assessing cellular biofouling. MRC5 and BxPC-3 were incubated on peptide-modified chips for 24 hours at 37 °C. After incubation, the chips were washed, and the adhered cells were immunostained. Fig. 6C and D depicts representative fluorescence images of the zwitterionic peptide-modified PSi, where no fluorescence is observed for both MRC5 and BxPC-3 cells. In contrast, these cells are observed to strongly adhere to the bare oxidized PSi surface (Fig. 6A and B).
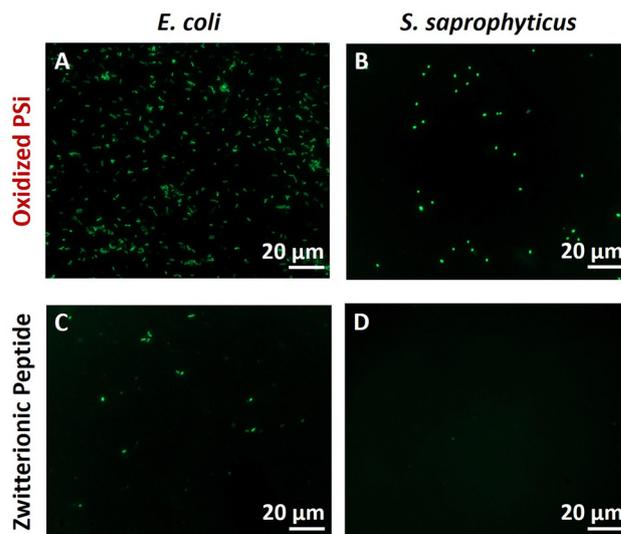

Fig. 5 Attachment and colonization of *E. coli* and *S. saprophyticus* bacteria to (A) and (B) bare oxidized PSi, and (C) and (D) zwitterionic peptide-immobilized PSi. Representative fluorescence microscopy images of the different surfaces following Syto9 staining.

Overall, the zwitterionic peptide-modified PSi surfaces demonstrated strong resistance to biofouling by both bacterial and mammalian cells. These findings confirm the broad-spectrum antibiofouling properties of the zwitterionic peptide coating, underscoring its potential to improve the performance and reliability of PSi-based biosensors in complex biological environments and implantable medical applications.
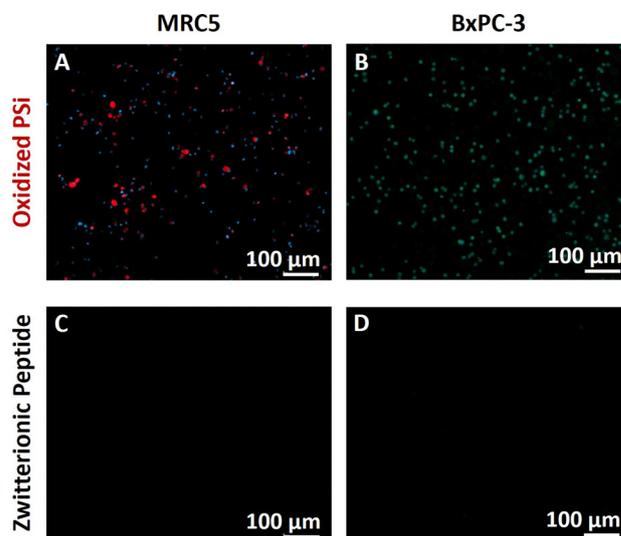

Fig. 6 Mammalian cell (MRC5 and BxPC-3) adhesion to (A) and (B) bare oxidized PSi, and (C) and (D) zwitterionic peptide-immobilized PSi. Representative fluorescence microscopy images of MRC5 stained with the Alexa fluor 647-conjugated anti-vimentin antibody (red, cytoskeleton) and counterstained with DAPI (blue, nuclei), and BxPC-3 cells stained with FITC-conjugated anti-EpCAM antibody (green, membrane marker) and DAPI.

Conclusions

This work demonstrates the potential of zwitterionic peptides with EK repeating motifs as an effective strategy for mitigating biofouling in PSi-based biosensors. Among the studied sequences, peptide 1 (EKEKEKEKEKGGC)-immobilized PSi exhibited superior resistance to protein adsorption, outperforming other peptides and conventional PEG modifications. The superior antibiofouling performance of peptide 1 was also demonstrated in complex biofluids such as bacterial lysate and GI fluids, where non-specific adsorption was effectively minimized.

Building on this strategy, we integrated the zwitterionic peptide as a passivation layer into a PSi-based aptasensor for lactoferrin detection and confirmed that aptamer functionality remained fully intact. In buffer, the peptide-modified aptasensor preserved the signal response seen with PEG passivation, while in complex GI fluids, it achieved substantially improved analytical performance. Specifically, the peptide-modified biosensor demonstrated an enhancement of more than an order of magnitude in both the LOD (49 *vs.* 600) and the SNR (40 *vs.* 0.4–1.7) values over the over the PEG-based design. This improvement enabled reliable detection of lactoferrin at clinically relevant concentrations, even under complex, interference-rich conditions.

Beyond protein resistance, zwitterionic peptides demonstrated strong potential in minimizing adhesion of bacteria and mammalian cells. Peptide 1 was tested against Gram-positive (*S. saprophyticus*) and Gram-negative (*E. coli*) bacteria after 24 hours of incubation on PSi surfaces. Bacterial adhesion was significantly reduced on the peptide-modified surface. Similarly, for mammalian cells, two different cell lines (MRC5 and BxPC-3) were tested, and in both cases, peptide 1 completely prevented cell adhesion.

These results underscore the potential of zwitterionic peptides with EK repeating motifs for mitigating biofouling across a range of targets, from small biomolecules and complex biofluids to bacterial and mammalian cells, and for enabling the development of sensitive, reliable PSi-based biosensors.

Experimental

Materials

Si wafers (highly doped p-type, ⟨100⟩-oriented, with a characteristic resistivity of ~0.95 mΩ cm) were obtained from Sil'tronix Silicon Technologies (Archamps, France). Absolute ethanol was provided by Bio-Lab Ltd (Jerusalem, Israel). Aqueous hydrofluoric acid (HF) 48%, *N*-hydroxysuccinimide (NHS), *N*-ethyldiisopropylamine (EDIPA), (3-aminopropyl) triethoxysilane (APTES), methoxypolyethylene glycol amine 750 Da (mPEG-NH$_2$), succinic anhydride, acetonitrile (ACN), *N*-(3-dimethylaminopropyl)-*N'*-ethylcarbodiimide hydrochloride (EDC), 2-(*n*-morpolino) ethanesulfonic acid (MES), MES sodium salt, Tris base, dithiothreitol (DTT), lactoferrin from bovine milk, trypsin, bovine serum albumin (BSA), Eagle's minimal essential medium (MEM) Earle's salts, fetal bovine serum

(FBS), penicillin streptomycin, sodium pyruvate, MEM non-essential amino acid solution, L-glutamine, Roswell Park Memorial Institute (RPMI) 1640 medium, Dulbecco's phosphate buffered saline (DPBS), Triton X100, 4′,6-diamidino-2-phenylindole (DAPI), Syto9 dye, and buffer salts were supplied by Sigma-Aldrich Chemicals (Rehovot, Israel). Methoxypolyethylene glycol thiol 750 Da (mPEG-SH) was obtained from Biopharma PEG Scientific Inc. (USA). Brain heart infusion (BHI) broth was supplied by Difco (USA). Paraformaldehyde (PFA) and the TrypLE express enzyme were supplied by Rhenium (Israel). The rabbit monoclonal Alexa fluor 647-labeled anti-vimentin antibody was generously supplied by Prof. Amit Zeisel, Technion. Mouse monoclonal anti-EpCAM was purchased from Bio-Rad (USA) and FITC-labeled anti-mouse antibodies were obtained from Jackson ImmunoResearch (USA). All peptides and FAM6-labeled peptides were obtained from PepMic (Suzhou, China); peptides were purchased with an acetylated N-terminus and an amidated C-terminus. Sulfo-*N*-ε-maleimidocaproyl-oxysulfosuccinimide ester (sulfo-EMCS) was supplied by Tzamal D-Chem Laboratories (Petach-Tikva, Israel). 3′-Thiol modified anti-LF aptamer Lac 9-2[70] (5′-CA GGC AGG ACA CCG TAA CCG GTG CAT CTA TGG CTA CTA GCT CTT CCT GCC TAT TTT TTT TTT-3′) was purchased from Integrated DNA Technologies (Coralville, USA).

Buffers. Phosphate buffered saline (PBS, pH 7.4) consisting of NaCl (137 mM), Na$_2$HPO$_4$ (10 mM), KCl (2.7 mM), and KH$_2$PO$_4$ (2 mM) was used. Selection buffer (SB, pH 7.4) was prepared by dissolving MgCl$_2$ in PBS (pH 7.4) to a concentration of 1 mM. Motility buffer (MB, pH 6.85) consisted of K$_2$HPO$_4$ (6.2 mM), KH$_2$PO$_4$ (3.8 mM), NaCl (67 mM), EDTA (0.1 mM), L-methionine (1 mM), and sodium lactate (10 mM). All buffer solutions were prepared using Milli-Q water (ddH$_2$O, 18.2 MΩ cm).

Cell lines. Human pancreatic cancer BxPC-3 cell line, human lung fibroblast MRC5 cell line, *Staphylococcus saprophyticus* (*S. saprophyticus*) ATCC 15305, and *Escherichia coli* (*E. coli*) ATCC 25922 were obtained from the American Type Culture Collection (ATCC).

Biofluids. Gastrointestinal (GI) fluids were supplied by Given Imaging Ltd. The GI fluids were obtained from domestic pigs, *Sus scrofa domesticus* (large White mixed with Landrace, aged 5.5 months and weighing 90 kg) from Lahav Research Institute according to ethic approval IL-17-8-290 (The Israel National Ethic Committee). *E. coli* lysates were prepared as previously described.[85]

PSi fabrication

Silicon anodization. PSi films were fabricated *via* anodization in an HF solution and ethanol, as previously described.[86,87] Two anodization conditions were used to produce PSi films: (1) applying a current density of 75 mA cm^{-2} for 70 s using a 1:1 (v/v) HF/ethanol solution, to produce films with 80-nm diameter pores and a layer thickness of 3 μm; (2) applying a current density of 15 mA cm^{-2} for 225 s using a 3:1 (v/v) HF/ethanol solution, resulting in films with 20-nm diameter pores and 2.5 μm thick. Following anodization, all films were

thermally oxidized at 800 °C for 1 h in a tube furnace (Lindberg/ Blue M 1200 °C Split-Hinge, Thermo Scientific, USA).

Peptide immobilization

Oxidized PSi films were first amino silanized by incubation in APTES (1% v/v) and EDIPA (1% v/v) solution in ddH$_2$O for 1 h, followed by extensive rinsing with ddH$_2$O and ethanol. Subsequently, annealing was performed at 100 °C for 15 min. Once cooled down to room temperature, the amino-silanized PSi was incubated in a solution of EMCS (5 mg mL^{-1}) in PBS for 1 h. The PSi films were then thoroughly washed with PBS and incubated for 1 h with the respective peptide solution in PBS at a concentration of 1.3 mM (equivalent to 1 mg mL^{-1} PEG). Finally, the films were treated with cysteine (50 mM in PBS) for 15 min. Table 1 lists the studied peptides and their characteristics in terms of molecular weight and isoelectric point values. PEG-terminated PSi films served as control, where following the EMCS activation the films were incubated in a solution of 1 mg mL^{-1} thiol-PEG (750 Da) for 1 h.

Characterization of peptide conjugation to the PSi surface

Fourier transform infrared (FTIR) spectroscopy. The synthetic steps followed for the peptide immobilization onto the PSi surface were characterized using attenuated total reflectance FTIR spectroscopy (Thermo 6700 FTIR equipped with a Smart iTR diamond ATR).

Water contact angle. Contact angle values of water droplets (7 μL) on the various modified PSi were measured using an Attension Theta Lite optical tensiometer (Biolin Scientific, Sweden). Digital images of the droplets on each substrate were acquired using a CCD camera and the respective contact angle was calculated using OneAttension Software using the Young–Laplace equation.

Confocal laser scanning microscopy (CLSM). FAM6-labeled peptide 1 was robotically spotted onto the PSi surface using an iTWO-300P microspotter device (M2-automation, Germany) equipped with a PDMD micro-dispenser. Spotting was performed at a voltage of 56 V, a peak duration of 59 μs and a frequency of 80 Hz, yielding droplets of ∼200 pL and a spot diameter of ∼300 μm. The spots were characterized by imaging using a confocal laser scanning microscope (LSM 880, Carl Zeiss, Inc.) linked to a Zeiss inverted microscope that was equipped with a Zeiss X63 oil immersion objective. FAM6-labeled peptides were excited with a laser line of 488 nm.

Protein and bio-fluid adsorption

The RIFTS method[88] was employed to evaluate protein adsorption in both buffer and biofluids on the different modified PSi films in real time. The PSi films are fixed in a custom flow cell, as described previously,[15] and the effective optical thickness (EOT) shifts due to biomolecule adsorption were monitored by fast Fourier transformation (FFT) analysis of reflectance spectra (in the wavelength range of 450–900 nm) acquired every 15 s.

In these experiments, PBS was first introduced for 30 min to acquire a stable baseline. Then, different protein solutions were introduced (BSA, LF, and AGR2 at a concentration of

1 mg mL^{-1}), as well as complex biofluids (GI fluids at 10 mg mL^{-1} and bacteria lysate at 2.5 mg mL^{-1}) and incubated for 1 h. Finally, the chips were washed with PBS for 30 min to remove unbound proteins and biomolecules.

The results are presented as the relative change in EOT (ΔEOT/EOT$_0$), calculated using the following equation:

$$\frac{\Delta EOT_t}{EOT_0} = \frac{EOT_t - EOT_0}{EOT_0}$$

where EOT$_0$ is the average EOT value during the PBS baseline, and EOT$_t$ is the EOT value at a given time point.

The antibiofouling properties of peptide 1 were also studied using a Quartz crystal microbalance (QCM-D). QCM SiO$_2$ sensors were purchased from (RenLux Crystal Ltd, China) and served as substrates for the protein adsorption assay. The sensors were functionalized similarly to PSi films (as described in the previous sections). In this set of experiments, a baseline was established with PBS for 30 min, followed by exposure to LF protein solutions at a concentration of 1 mg mL^{-1} for 1 h. Subsequently, the sensors were washed with PBS for 30 min to remove loosely bound proteins. All QCM experiments were conducted at a flow rate of 20 μl min^{-1}.

Biosensing experiments for the detection of lactoferrin

PSi functionalization with aptamers. APTES-modified PSi surfaces were first activated with the EMCS crosslinker (5 mg mL^{-1} in PBS) for 1 h. After washing, the surfaces were incubated with 3′-thiol-modified anti-LF aptamer Lac 9-2[70] (30 μM in PBS) for 1 h. Remaining EMCS groups were then deactivated by incubation with zwitterionic peptides, as described in the peptide conjugation section.

Characterization of aptamer conjugation. The RIFTS method, described before, was employed to confirm aptamer conjugation to the amino-silanized PSi. PBS was first introduced to establish a stable baseline, after which the different chemical solutions were introduced and incubated according to the conjugation protocol. After each step, the sample was thoroughly washed with PBS to remove unbound molecules.

In addition, Cy5-labeled aptamers were immobilized on the PSi surface, followed by imaging using a CLSM (LSM 880, Carl Zeiss, Inc.) coupled to a Zeiss inverted microscope equipped with a X63 oil immersion objective. PSi photoluminescence (PL) and Cy5 fluorescence were excited at 405 nm and 639 nm, respectively. To generate a 3D projection of the porous structure, z-stack images were acquired at 0.3 μm intervals over a depth of ∼3 μm. Image processing and analysis were performed using Imaris Bitplane scientific software.

Biosensing experiments. Biosensing experiments were performed as described previously.[15] Briefly, the aptasensor was mounted in a custom-made flow cell, and the reflectivity spectra were recorded every 15 s. For buffer experiments, aptamers were unfolded with elution buffer, refolded in selection buffer (SB), followed by incubation with protein solution and washing in SB. For GI fluid experiments, sensors were preequilibrated in SB and then exposed to neat and spiked GI fluids, with incubations and washes at 37 °C. The binding curve

in the GI fluid was obtained using separate PSi aptasensors for each LF concentration. The results are presented as a relative ΔEOT.

Signal-to-noise ratio (SNR) values were determined by calculating the ratio of the net relative EOT signal to the standard deviation (σ) of the baseline signal prior to protein introduction. The limit of detection (LOD) was defined as the concentration corresponding to a signal equal to three times the baseline standard deviation (3σ).

Bacterial attachment

Bacterial cell cultures. *E. coli* and *S. saprophyticus* were retrieved from $-80\ ^\circ$C stocks by streaking onto BHI agar plates separately and then incubated overnight at $37\ ^\circ$C. A single formed colony of each bacterial strain was transferred to 5 mL BHI medium and grown overnight at $37\ ^\circ$C with spinning, followed by sub-culturing in a 1:100 dilution in fresh BHI medium for 3 hours. Bacterial cells were harvested by centrifugation at $2580 \times g$ for 5 min at room temperature, washed twice with PBS, and then resuspended in PBS in order to achieve an optical density measured of 0.1, corresponding to 10^7 CFU mL^{-1}.

Bacterial adhesion assay. PSi chips anodized at 75 mA cm^{-2} for 70 s were sterilized prior to the experiment. Bacterial suspensions were then introduced and incubated for 24 h at $37\ ^\circ$C. Post-incubation chips were gently rinsed three times with PBS, followed by 30 min of shaking to remove loosely adhered cells. Adhered bacteria were stained with the 0.1% (v/v) Syto9 dye in PBS, by incubating the PSi in the dye solution for 1 h at room temperature in the dark. The samples were washed with PBS and dried under nitrogen steam prior to characterization by fluorescence microscopy (Zeiss Axioscope 7, Germany, equipped with Objective EC Epiplan X20/0.4 and Objective EC Epiplan X50/0.7 objective), and the excitation wavelength was 488 nm for Syto9.

Mammalian cell adhesion

Cell culture and harvest. BxPC-3 and MRC5 cells were cultured in T-75 flasks (Thermo-Fisher) at $37\ ^\circ$C in a humidified atmosphere of 5% CO$_2$. BxPC-3 was cultured in RPMI medium containing 10% FBS and 1% penicillin streptomycin. MRC5 was cultured in MEM medium supplemented with 10% FBS, 1% penicillin streptomycin, 1 mM sodium pyruvate, 1% MEM non-essential amino acid solution, and 4 mM ʟ-glutamine solution. Cells were harvested for experiments once they reached 90% confluency. First, adhered cells were harvested using TrypLE and then resuspended in DPBS to achieve a final concentration of 2×10^5 cells mL^{-1}.

Cell adhesion assay. PSi chips anodized at 15 mA cm^{-2} for 225 s were UV-treated for 30 min, incubated in DPBS, and seeded with cells. After 24 h incubation at $37\ ^\circ$C and 5% CO$_2$, chips were gently rinsed with DPBS to remove loosely adhered cells. Adhered cells were fixed with 4% PFA solution for 10 min, permeabilized with 0.2% Triton X100 in DPBS for 2 min and blocked with 5% BSA for 1 h. BxPC-3 cells were stained with the anti-EpCAM primary antibody for 2 h at room temperature,

followed by the FITC-labeled secondary antibody for 1 h. MRC5 cells were stained overnight at $4\ ^\circ$C with the Alexa fluor 647-labeled anti-vimentin antibody, followed by counterstaining with DAPI (1 µg mL^{-1}) for 15 min. Finally, the chips were mounted using a ProLong mountant for further examination under the microscope. The adhered cells on the PSi chips were examined under a microscope (Zeiss Axioscope 7, Germany, equipped with a Zeiss X20/0.4 objective). Excitation wavelengths were 353 nm for DAPI, 488 nm for FITC, and 653 nm for Alexa fluor 647.

Statistical analysis

All experiments were repeated at least three times. The data are presented as the mean ($n \geq 3$) with the standard deviation. For statistical analysis, an unpaired *t*-test with two-tailed distribution and unequal variance was used. A *p*-value of less than 0.05 was considered statistically significant.

Author contributions

Kayan Awawdeh: conceptualization, methodology, investigation, formal analysis, visualization, and writing (original draft preparation). Xin Jiang and Lisa Dahan: investigation and writing (review and editing). Matan Atias: investigation. Janina Bahnemann: methodology, funding acquisition, and writing (review and editing). Ester Segal: conceptualization, formal analysis, supervision, funding acquisition and writing (review and editing).

Conflicts of interest

There are no conflicts to declare.

Data availability

The data supporting this article have been included as part of the SI. Supplementary information includes PSi surface characterization, peptide conjugation characterization and quantification, as well as protein adsorption analysis on different surfaces using reflective interferometric Fourier transform spectroscopy (RIFTS) and quartz crystal microbalance (QCM). See DOI: **https://doi.org/10.1039/d5nh00478k**.

Any additional data are available upon request from the authors.

Acknowledgements

References

1 R. G. Chapman, et al., Surveying for Surfaces that Resist the Adsorption of Proteins, J. Am. Chem. Soc., 2000, **122**, 8303–8304.

2 E. Ostuni, R. G. Chapman, R. E. Holmlin, S. Takayama and G. M. Whitesides, A Survey of Structure–Property Relationships of Surfaces that Resist the Adsorption of Protein, Langmuir, 2001, **17**, 5605–5620.

3 J. Y. Lichtenberg, Y. Ling and S. Kim, Non-Specific Adsorption Reduction Methods in Biosensing, Sensors, 2019, **19**, 2488.

4 R. Sánchez-Salcedo, P. Sharma and N. H. Voelcker, Advancements in Porous Silicon Biosensors for Point of Care, Wearable, and Implantable Applications, ACS Appl. Mater. Interfaces, 2025, **17**, 2814–2843.

5 S. Arshavsky-Graham, et al., Aptamers vs. antibodies as capture probes in optical porous silicon biosensors, Analyst, 2020, **145**, 4991–5003.

6 R. Salama, S. Arshavsky-Graham, O. Sella-Tavor, N. Massad-Ivanir and E. Segal, Design considerations of aptasensors for continuous monitoring of biomarkers in digestive tract fluids, Talanta, 2022, **239**, 123124.

7 N. R. Nirala, J. Asiku, H. Dvir and G. Shtenberg, N-acetyl-β-D-glucosaminidase activity assay for monitoring insulin-dependent diabetes using Ag-porous Si SERS platform, Talanta, 2022, **239**, 123087.

8 R. Vercauteren, A. Leprince, M. Nuytten, J. Mahillon and L. A. Francis, Indirect Detection of Bacteria on Optically Enhanced Porous Silicon Membrane-Based Biosensors Using Selective Lytic Enzymes, ACS Sens., 2023, **8**, 2627–2634.

9 C. Pacholski, M. Sartor, M. J. Sailor, F. Cunin and G. M. Miskelly, Biosensing Using Porous Silicon Double-Layer Interferometers: Reflective Interferometric Fourier Transform Spectroscopy, J. Am. Chem. Soc., 2005, **127**, 11636–11645.

10 D. Silva de Vasconcellos, et al., Process for integrating multiple porous silicon membranes with variable characteristics into planar microfluidics, Sens. Actuators, A, 2024, **377**, 115715.

11 E. Mäkilä, et al., Influence of Surface Chemistry on Ibuprofen Adsorption and Confinement in Mesoporous Silicon Microparticles, Langmuir, 2016, **32**, 13020–13029.

12 W. A. Tárraga, A. S. Picco and G. S. Longo, Understanding protein adsorption on silica mesoporous materials through thermodynamic simulations, Surf. Interfaces, 2024, **52**, 104870.

13 D. M. Schlipf, S. E. Rankin and B. L. Knutson, Pore-size dependent protein adsorption and protection from proteolytic hydrolysis in tailored mesoporous silica particles, ACS Appl. Mater. Interfaces, 2013, **5**, 10111–10117.

14 J. Patel, et al., Electrochemical properties of nanostructured porous gold electrodes in biofouling solutions, Anal. Chem., 2013, **85**, 11610–11618.

15 K. Awawdeh, M. A. Buttkewitz, J. Bahnemann and E. Segal, Enhancing the performance of porous silicon biosensors: the interplay of nanostructure design and microfluidic integration, Microsyst. Nanoeng., 2024, **10**, 100.

16 S. A. Rodríguez-Montelongo, et al., Porous Silicon-Based DNA Biosensor for Human Papillomavirus Detection: Towards the Design of Fast and Portable Test, Silicon, 2023, **15**, 2371–2383.

17 S. B. Nimse, M. D. Sonawane, K. S. Song and T. Kim, Biomarker detection technologies and future directions, Analyst, 2016, **141**, 740–755.

18 N. I. Al-Dewik, S. N. Younes, M. M. Essa, S. Pathak and M. W. Qoronfleh, Making Biomarkers Relevant to Healthcare Innovation and Precision Medicine, Processes, 2022, **10**, 1107.

19 W. M. De Vos, F. A. M. Leermakers, A. De Keizer, M. A. C. Stuart and J. M. Kleijn, Field theoretical analysis of driving forces for the uptake of proteins by like-charged polyelectrolyte brushes: Effects of charge regulation and patchiness, Langmuir, 2010, **26**, 249–259.

20 M. Rabe, D. Verdes and S. Seeger, Understanding protein adsorption phenomena at solid surfaces, Adv. Colloid Interface Sci., 2011, **162**, 87–106.

21 S. Arshavsky-Graham, N. Massad-Ivanir, E. Segal and S. Weiss, Porous Silicon-Based Photonic Biosensors: Current Status and Emerging Applications, Anal. Chem., 2019, **91**, 441–467.

22 R. H. Kang, S. W. Baek, C.-K. Oh, Y. H. Kim and D. Kim, Recent Advances of Macrostructural Porous Silicon for Biomedical Applications, ACS Appl. Mater. Interfaces, 2025, **17**, 5609–5626.

23 K. Urmann, et al., Rapid and label-free detection of protein a by aptamer-tethered porous silicon nanostructures, J. Biotechnol., 2017, **257**, 171–177.

24 S. Arshavsky-Graham, et al., Porous Silicon-Based Aptasensors: Toward Cancer Protein Biomarker Detection, ACS Meas. Sci. Au, 2021, **1**, 82–94.

25 T. Cao, Y. Zhao, C. A. Nattoo, R. Layouni and S. M. Weiss, A smartphone biosensor based on analysing structural colour of porous silicon, Analyst, 2019, **144**, 3942–3948.

26 D. N. Kumar, Z. Baider, D. Elad, S. E. Blum and G. Shtenberg, Botulinum Neurotoxin C Dual Detection through Immunological Recognition and Endopeptidase Activity Using Porous Silicon Interferometers, Anal. Chem., 2022, **94**, 5927–5936.

27 C. Jiang, et al., Antifouling Strategies for Selective In Vitro and In Vivo Sensing, Chem. Rev., 2020, **120**, 3852–3889.

28 E. Moore, et al., Surface-initiated hyperbranched polyglycerol as an ultralow-fouling coating on glass, silicon, and

porous silicon substrates, *ACS Appl. Mater. Interfaces*, 2014, **6**, 15243–15252.

29 D. Wilms, S.-E. Stiriba and H. Frey, Hyperbranched Polyglycerols: From the Controlled Synthesis of Biocompatible Polyether Polyols to Multipurpose Applications, *Acc. Chem. Res.*, 2010, **43**, 129–141.

30 C. K. Tsang, T. L. Kelly, M. J. Sailor and Y. Y. Li, Highly Stable Porous Silicon–Carbon Composites as Label-Free Optical Biosensors, *ACS Nano*, 2012, **6**, 10546–10554.

31 J. Salonen and E. Mäkilä, Thermally Carbonized Porous Silicon and Its Recent Applications, *Adv. Mater.*, 2018, **30**, 1703819.

32 R. Layouni, M. H. Choudhury, P. E. Laibinis and S. M. Weiss, Thermally Carbonized Porous Silicon for Robust Label-Free DNA Optical Sensing, *ACS Appl. Bio Mater.*, 2020, **3**, 622–627.

33 G. P. Chin, K. Guo, R. Vasani, N. H. Voelcker and B. Prieto-Simón, Carbon-stabilized porous silicon biosensor for the ultrasensitive label-free electrochemical detection of bacterial RNA gene fragments, *Biosens. Bioelectron.: X*, 2024, **16**, 100438.

34 J. Rytkönen, *et al.*, Functionalization of mesoporous silicon nanoparticles for targeting and bioimaging purposes, *J. Nanomater.*, 2012, **2012**, 6–8.

35 B. Sciacca, S. D. Alvarez, F. Geobaldo and M. J. Sailor, Bioconjugate functionalization of thermally carbonized porous silicon using a radical coupling reaction, *Dalton Trans.*, 2010, **39**, 10847.

36 S. Moayedi, W. Xia, L. Lundergan, H. Yuan and J. Xu, Zwitterionic Polymers for Biomedical Applications: Antimicrobial and Antifouling Strategies toward Implantable Medical Devices and Drug Delivery, *Langmuir*, 2024, **40**, 23125–23145.

37 Q. Li, *et al.*, Zwitterionic Biomaterials, *Chem. Rev.*, 2022, **122**, 17073–17154.

38 L. Zheng, H. S. Sundaram, Z. Wei, C. Li and Z. Yuan, Applications of zwitterionic polymers, *React. Funct. Polym.*, 2017, **118**, 51–61.

39 A. Venault and Y. Chang, Designs of Zwitterionic Interfaces and Membranes, *Langmuir*, 2019, **35**, 1714–1726.

40 P. Losada-Pérez, O. Polat, A. N. Parikh, E. Seker and F. U. Renner, Engineering the interface between lipid membranes and nanoporous gold: A study by quartz crystal microbalance with dissipation monitoring, *Biointerphases*, 2018, **13**, 011002.

41 S. M. Smail, P. E. Laibinis and S. M. Weiss, Baseline Stability of Thermally Hydrosilated Porous Silicon with Zwitterionic Antifouling Polymer Coating for Biosensing Applications, *ACS Omega*, 2025, **10**, 31932–31939.

42 G. Wang, *et al.*, Zwitterionic peptide anchored to conducting polymer PEDOT for the development of antifouling and ultrasensitive electrochemical DNA sensor, *Biosens. Bioelectron.*, 2017, **92**, 396–401.

43 Z. Song, *et al.*, Designed zwitterionic peptide combined with sacrificial Fe-MOF for low fouling and highly sensitive electrochemical detection of T4 polynucleotide kinase, *Sens. Actuators, B*, 2020, **305**, 127329.

44 H. Chen, *et al.*, Enhanced Anti-Interference Photoelectrochemical DNA Bioassay: Grafting a Peptide-Conjugated Hairpin DNA Probe on a COF-Based Photocathode, *ACS Sens.*, 2025, **10**, 507–516.

45 C. Li, *et al.*, Lubricin-Inspired Loop Zwitterionic Peptide for Fabrication of Superior Antifouling Surfaces, *ACS Appl. Mater. Interfaces*, 2021, **13**, 41978–41986.

46 M. Cui, *et al.*, Antifouling sensors based on peptides for biomarker detection, *TrAC, Trends Anal. Chem.*, 2020, **127**, 115903.

47 C. Overby, S. Park, A. Summers and D. S. W. Benoit, Zwitterionic peptides: Tunable next-generation stealth nanoparticle modifications, *Bioact. Mater.*, 2023, **27**, 113–124.

48 Z. Cui, Y. Wang, L. Zhang and H. Qi, Zwitterionic Peptides: From Mechanism, Design Strategies to Applications, *ACS Appl. Mater. Interfaces*, 2024, **16**, 56497–56518.

49 J. Cui, *et al.*, Nanoscale engineering of low-fouling surfaces through polydopamine immobilisation of zwitterionic peptides, *Soft Matter*, 2014, **10**, 2656–2663.

50 T. Ederth, M. Lerm, B. Orihuela and D. Rittschof, Resistance of Zwitterionic Peptide Monolayers to Biofouling, *Langmuir*, 2019, **35**, 1818–1827.

51 S. Chen, Z. Cao and S. Jiang, Ultra-low fouling peptide surfaces derived from natural amino acids, *Biomaterials*, 2009, **30**, 5892–5896.

52 A. K. Nowinski, F. Sun, A. D. White, A. J. Keefe and S. Jiang, Sequence, Structure, and Function of Peptide Self-Assembled Monolayers, *J. Am. Chem. Soc.*, 2012, **134**, 6000–6005.

53 A. D. White, *et al.*, Decoding nonspecific interactions from nature, *Chem. Sci.*, 2012, **3**, 3488–3494.

54 R. K. Das and R. V. Pappu, Conformations of intrinsically disordered proteins are influenced by linear sequence distributions of oppositely charged residues, *Proc. Natl. Acad. Sci. U. S. A.*, 2013, **110**, 13392–13397.

55 S. Mariani, L. Pino, L. M. Strambini, L. Tedeschi and G. Barillaro, 10 000-Fold Improvement in Protein Detection Using Nanostructured Porous Silicon Interferometric Aptasensors, *ACS Sens.*, 2016, **1**, 1471–1479.

56 S. Ciampi, J. B. Harper and J. J. Gooding, Wet chemical routes to the assembly of organic monolayers on silicon surfaces via the formation of Si–C bonds: surface preparation, passivation and functionalization, *Chem. Soc. Rev.*, 2010, **39**, 2158–2183.

57 C. Song, *et al.*, Peptide-Conjugated Fluorescent Silicon Nanoparticles Enabling Simultaneous Tracking and Specific Destruction of Cancer Cells, *Anal. Chem.*, 2015, **87**, 6718–6723.

58 M. Cui, *et al.*, Mixed Self-Assembled Aptamer and Newly Designed Zwitterionic Peptide as Antifouling Biosensing Interface for Electrochemical Detection of alpha-Fetoprotein, *ACS Sens.*, 2017, **2**, 490–494.

59 H. Leonard, *et al.*, Shining light in blind alleys: deciphering bacterial attachment in silicon microstructures, *Nanoscale Horiz.*, 2022, **7**, 729–742.

60 M. Li, B. Zhuang and J. Yu, Sequence-Conformation Relationship of Zwitterionic Peptide Brushes: Theories and Simulations, *Macromolecules*, 2021, **54**, 9565–9576.

61 P. McMullen, *et al.*, Motif-based zwitterionic peptides impact their structure and immunogenicity, *Chem. Sci.*, 2022, **13**, 10961–10970.

62 C. Li, *et al.*, Structures and Antifouling Properties of Self-Assembled Zwitterionic Peptide Monolayers: Effects of Peptide Charge Distributions and Divalent Cations, *Biomacromolecules*, 2020, **21**, 2087–2095.

63 R. Moretta, *et al.*, PNA-Based Graphene Oxide/Porous Silicon Hybrid Biosensor: Towards a Label-Free Optical Assay for Brugada Syndrome, *Nanomaterials*, 2020, **10**, 2233.

64 J. Abramson, *et al.*, Accurate structure prediction of biomolecular interactions with AlphaFold 3, *Nature*, 2024, **630**, 493–500.

65 Y. Li, *et al.*, Biomimetic functional material-based sensors for food safety analysis: A review, *Food Chem.*, 2023, **405**, 134974.

66 Y. Li, *et al.*, Engineering an antifouling electrochemical aptasensor based on a designed zwitterionic peptide for tetracycline detection in milk, *Food Control*, 2023, **153**, 109929.

67 E. F. Pettersen, *et al.*, UCSF ChimeraX: Structure visualization for researchers, educators, and developers, *Protein Sci.*, 2021, **30**, 70–82.

68 E. Hamed, T. Xu and S. Keten, Poly(ethylene glycol) conjugation stabilizes the secondary structure of α-helices by reducing peptide solvent accessible surface area, *Biomacromolecules*, 2013, **14**, 4053–4060.

69 I. A. Imam, *et al.*, Integrating Protein Language Model and Molecular Dynamics Simulations to Discover Antibiofouling Peptides, *Langmuir*, 2025, **41**, 811–821.

70 W. Jia, *et al.*, Silver decahedral nanoparticles empowered SPR imaging-SELEX for high throughput screening of aptamers with real-time assessment, *Biosens. Bioelectron.*, 2018, **109**, 206–213.

71 S. S. Fedail, R. F. Harvey, P. R. Salmon, P. Brown and A. E. Read, Trypsin and lactoferrin levels in pure pancreatic juice in patients with pancreatic disease, *Gut*, 1979, **20**, 983–986.

72 M. Kayazawa, Lactoferrin in whole gut lavage fluid as a marker for disease activity in inflammatory bowel disease: comparison with other neutrophil-derived proteins, *Am. J. Gastroenterol.*, 2002, **97**, 360–369.

73 S. S. Fedail, P. R. Salmon, R. F. Harvey and A. E. Read, Radioimmunoassay of lactoferrin in pancreatic juice as a test for pancreatic diseases, *Lancet*, 1978, **311**, 181–182.

74 L. Multigner, C. Figarella and H. Sarles, Diagnosis of chronic pancreatitis by measurement of lactoferrin in duodenal juice, *Gut*, 1981, **22**, 350–354.

75 J. Hegnhøj and O. B. S. De Muckadell, An enzyme linked immunosorbent assay for measurements of lactoferrin in duodenal aspirates and other biological fluids, *Scand. J. Clin. Lab. Invest.*, 1985, **45**, 489–495.

76 X. Jiang, *et al.*, Accurate Prediction of Antimicrobial Susceptibility for Point-of-Care Testing of Urine in Less than 90 Minutes via iPRISM Cassettes, *Adv. Sci.*, 2023, **10**, 1–14.

77 M. Corsi, *et al.*, In vivo and in situ monitoring of doxorubicin pharmacokinetics with an implantable bioresorbable optical sensor, *Sci. Adv.*, 2025, **11**, 1–15.

78 O. U. Lawal, *et al.*, Staphylococcus saprophyticus From Clinical and Environmental Origins Have Distinct Biofilm Composition, *Front. Microbiol.*, 2021, **12**, 1–13.

79 Z. Khatoon, C. D. McTiernan, E. J. Suuronen, T.-F. Mah and E. I. Alarcon, Bacterial biofilm formation on implantable devices and approaches to its treatment and prevention, *Heliyon*, 2018, **4**, e01067.

80 V. Ballén, V. Cepas, C. Ratia, Y. Gabasa and S. M. Soto, Clinical Escherichia coli: From Biofilm Formation to New Antibiofilm Strategies, *Microorganisms*, 2022, **10**, 1103.

81 P. Li, R. Yin, J. Cheng and J. Lin, Bacterial Biofilm Formation on Biomaterials and Approaches to Its Treatment and Prevention, *Int. J. Mol. Sci.*, 2023, **24**, 11680.

82 O. Prinz Setter, X. Jiang and E. Segal, Rising to the surface: capturing and detecting bacteria by rationally-designed surfaces, *Curr. Opin. Biotechnol.*, 2023, **83**, 102969.

83 S. Zheng, *et al.*, Implication of Surface Properties, Bacterial Motility, and Hydrodynamic Conditions on Bacterial Surface Sensing and Their Initial Adhesion, *Front. Bioeng. Biotechnol.*, 2021, **9**, 1–22.

84 A. Tzur-Balter, A. Gilert, N. Massad-Ivanir and E. Segal, Engineering porous silicon nanostructures as tunable carriers for mitoxantrone dihydrochloride, *Acta Biomater.*, 2013, **9**, 6208–6217.

85 K. Urmann, J.-G. Walter, T. Scheper and E. Segal, Label-Free Optical Biosensors Based on Aptamer-Functionalized Porous Silicon Scaffolds, *Anal. Chem.*, 2015, **87**, 1999–2006.

86 M. J. Sailor, *Porous silicon in practice: preparation, characterization and applications*, John Wiley & Sons, 2012.

87 Z. A. A. Hameed and F. A. H. Mutlak, Study the Effect of Changing the Etching Current in a Si Nanostructure to Improve the Spectral Sensitivity of the Detector, *Plasmonics*, 2024, **19**, 417–428.

88 E. Segal, *et al.*, Confinement of Thermoresponsive Hydrogels in Nanostructured Porous Silicon Dioxide Templates, *Adv. Funct. Mater.*, 2007, **17**, 1153–1162.